nature communications

Article

https://doi.org/10.1038/s41467-024-51147-6

Electronic cooling and energy harvesting using ferroelectric polymer composites

Received: 27 February 2024

Accepted: 29 July 2024

Published online: 06 August 2024

Check for updates

Kailun Zou[1,5], Peijia Bai[2,5], Kanghua Li[1], Fangyuan Luo[1], Jiajie Liang[3], Ling Lin[1], Rujun Ma[2] ✉, Qi Li[3] ✉, Shenglin Jiang[1], Qing Wang[4] ✉ & Guangzu Zhang[1] ✉

Thermal management emerges as a grand challenge of next-generation electronics. Efforts to develop compact, solid-state cooling devices have led to the exploration of the electrocaloric effect of ferroelectric polymers. Despite recent advances, the applications of electrocaloric polymers on electronics operating at elevated temperatures remain essentially unexplored. Here, we report that the ferroelectric polymer composite composed of highly-polarized barium strontium titanate nanofibers and electron-accepting [6,6] phenyl-C61-butyric acid methyl ester retains fast electrocaloric responses and stable cyclability at elevated temperatures. We demonstrate the effectiveness of electrocaloric cooling in a polymer composite for a pyroelectric energy harvesting device. The device utilizes a simulated central processing unit (CPU) as the heat source. Our results show that the device remains operational even when the CPU is overheated. Furthermore, we show that the composite functions simultaneously as a pyroelectric energy converter to harvest thermal energy from an overheated chip into electricity in the electrocaloric process. This work suggests a distinct approach for overheating protection and recycling waste heat of microelectronics.

The rising demands for highly-integrated compact electronics and electrical systems, coupled with their ever-increasing switching frequencies and power densities, give rise to an exponential increase in heat flux within devices and thus pose a critical challenge to current thermal management strategies for electronics[1–3]. The heat dissipation capabilities and cooling efficiencies of conventional air and liquid cooling and heat pipes are limited and unable to meet the increasing thermal control requirements of integrated circuits[4–6]. The conventional air/liquid cooling and heat pipes also suffer from large volume and complex structure since extra units are needed to drive the circulation of air or liquid[7,8], while thermoelectric cooling based on the Peltier effect suffers from low efficiency and coefficient of performance (COP) (Supplementary Table 1 and Supplementary Note 1). It has been shown that over 55% of electronic failures are attributable to heat accumulation and localized overheating due to insufficient thermal management[1,9]. Effective cooling is therefore critical for next-generation electronic devices to meet their stability, reliability and lifespan needs.

Solid-state refrigeration based on the caloric effects, including magnetocaloric, elasto/baro-caloric, and electrocaloric (EC) effects present attractive cooling strategies owing to their superior energy efficiency, zero greenhouse emissions and high reliability[10,11]. Among these disruptive technologies, EC refrigeration possesses unique features, such as direct use of electricity and compact configuration, and thus offers great potential for on-chip thermal management of electronic devices[12–16]. The electrocaloric effect (ECE) refers to the reversible thermal changes including adiabatic temperature change (ΔT) and isothermal entropy change (ΔS) of a ferroelectric material upon the application and removal of an electric field. Pronounced ECE

[1]School of Integrated Circuits, Huazhong University of Science and Technology, Wuhan, China. [2]School of Materials Science and Engineering, National Institute for Advanced Materials, Nankai University, Tianjin, China. [3]State Key Laboratory of Power System, Department of Electrical Engineering, Tsinghua University, Beijing, China. [4]Department of Materials Science and Engineering, The Pennsylvania State University, University Park, PA, USA. [5]These authors contributed equally: Kailun Zou, Peijia Bai. ✉e-mail: malab@nankai.edu.cn; qili1020@tsinghua.edu.cn; wang@matse.psu.edu; zhanggz@hust.edu.cn

has been recently obtained in ferroelectric ceramics, polymers and composites. For example, a new benchmark for EC ceramics has been established in the multilayered $PbSc_{0.5}Ta_{0.5}O_3$ with a ΔT of 5.5 °C near room temperature[17,18]. In addition to their intrinsic processability, scalability, weight and cost advantages, ferroelectric polymers represented by poly(vinylidene fluoride-*co*-trifluoroethylene) [P(VDF-TrFE)] and poly(vinylidene fluoride-*ter*-trifluoroethylene-*ter*-chlorofluoroethylene) [P(VDF-TrFE-CFE)] exhibit high breakdown strength and large EC effect[19–22]. Despite notable progress, the adoption of the current EC polymers and composites in microelectronics is hindered by their limited operating temperatures, which are typically lower than 50 °C[23,24]. The use of EC devices on working electronics at elevated temperatures has not been demonstrated. The Joule heat arises from exponentially increased electrical conduction with the applied field and temperature offsets the cooling energy of the ECE[13,18,25–28]

Here, we describe the introduction of barium strontium titanate nanofibers (BST NFs) and [6,6] phenyl-C61-butyric acid methyl ester (PCBM) into P(VDF-TrFE-CFE) to improve the ECE of the polymer while restraining electrical conduction to minimize energy loss from Joule heating at high fields and temperatures. In this composite strategy, BST NFs modulate the crystallization and polarization behaviors of the polymer through the ceramic-polymer interfacial coupling effect for high ECE[23] (Supplementary Note 2), and meanwhile, PCBM engineers the energy band for high electrically insulating performance. The polymer composite exhibit giant ECE, i.e., ΔT of 18.0 °C and ΔS of 0.170 J cm^{-3}°C^{-1}, over a wide temperature range of 0–80 °C and display an excellent cyclability over 100,000 cycles with an applied field of 150 MV m^{-1} at 80 °C. We demonstrate the simultaneous operation of EC cooling and electronics and a reduction of the CPU temperature from 80 to 42 °C using the polymer composite. Moreover, we show the polymer composite simultaneously functions as a pyroelectric energy converter to recycle the absorbed heat from electronics in the EC process into electricity. The pyroelectric energy conversion density of 1.33 J cm^{-3} achieved from an overheated chip with a surface temperature of 75 °C with the polymer composite outperforms those of the current pyroelectric ceramics and polymers.

Results

Material design and dielectric properties

The ternary polymer composites are composed of BST NFs (1/3 $Ba_{0.67}Sr_{0.33}TiO_3$ + 1/3 $Ba_{0.70}Sr_{0.30}TiO_3$ + 1/3 $Ba_{0.74}Sr_{0.26}TiO_3$ with various Curie temperatures, Supplementary Fig. 1) and PCBM dispersed in P(VDF-TrFE-CFE) matrix (Supplementary Figs. 2–5). Ferroelectric BST NFs with a high aspect ratio were added to enhance the polarization, ECE and pyroelectricity of the polymer, while PCBM was introduced to improve the electrical resistance and reduce conduction loss. For comparison purposes, the binary polymer composite BST/P(VDF-TrFE-CFE) and PCBM/P(VDF-TrFE-CFE) were prepared and characterized. The relaxor nature of P(VDF-TrFE-CFE) and its composites is evidenced by a shift of broad dielectric peaks toward high temperature with the increase of frequency in the dielectric spectra (Fig. 1a and Supplementary Fig. 6). The dielectric constant and polarization (P) of the composites increases with the contents of BST NFs (Fig. 1a–c and Supplementary Figs. 7–10). Moreover, the composites show decreased P with increasing temperature (T), e.g., the P of the polymer decreases from 0.039 C m^{-2} to 0.029 C m^{-2} when temperature increases from 20 to 80 °C, while the corresponding change of P of the binary composite with 9 vol.% BST NFs is from 0.102 C m^{-2} to 0.066 C m^{-2} (Fig. 1d and Supplementary Fig. 10). The higher $|\partial P/\partial T|$ of the composites is indicative of their improved EC and pyroelectric effects (Supplementary Fig. 11) compared to the pristine polymer[29–34].

While the low content of PCBM has a negligible impact on crystallization behavior (Supplementary Fig. 7 and Supplementary Table 2) and the dielectric properties (*i.e.*, dielectric constant and P) of the composites, it significantly decreases the hysteresis of the polarization-electric field (P-E) loops of the composites, especially at high temperatures (Fig. 1b and Supplementary Fig. 10), as a consequence of impeded electrical conduction, which has been confirmed by the resistivity measurements (Fig. 1e and Supplementary Fig. 12). For example, at 80 °C, the resistivity decreases from 5.5 × 10^9 Ω·m of the polymer to 8.9 × 10^8 Ω·m of the binary composite with 9 vol% BST NFs and increases markedly to 1.9 × 10^{11} Ω·m of the ternary composites with 0.75 vol% PCBM. As evaluated by the ultraviolet-visible (UV-vis) and ultraviolet photoelectron (UPS) spectroscopy (Supplementary Fig. 13a–f), PCBM has a higher electron affinity of 4.07 eV and a lower Fermi energy of 4.22 eV compared to P(VDF-TrFE-CFE) with an electron affinity of 2.05 eV and a Fermi level of 5.42 eV (Fig. 2a). Consequently, PCBM and P(VDF-TrFE-CFE) create a large energy barrier ($\Delta E_a + \Delta E_b$) of 3.22 eV to capture and trap charges (Fig. 2b). As shown by in-situ Kelvin probe force microscopy[35,36], the surface potential signal around BST NFs in the binary composite forms a distinct halo, indicating large amounts of charges accumulated at the interface. On the other hand, the surface potential around BST NFs in the ternary composite is nearly the same as the matrix, implying a homogenous distribution of space charge in the sample (Fig. 2c–f and Supplementary Fig. 14). This result clearly shows the benefit of using PCBM, which originates from eliminating the local hot spots of increased charge concentration and thus positively affecting the insulating properties of the composite. Interestingly, the resistivity of the composite enhanced by PCBM retains at high temperatures (Supplementary Fig. 12). In stark contrast, the resistivity of the BST/P(VDF-TrFE-CFE) binary composite decreases dramatically with increasing temperature, e.g., from 5.4 × 10^9 Ω·m at 20 °C to 8.9 × 10^8 Ω·m at 80 °C (Fig. 1e and Supplementary Fig. 12).

Moreover, the addition of PCBM successfully recovers the loss in the breakdown strength stemming from the introduced BST NFs. The breakdown strength increases from 271 MV m^{-1} of the BST (9 vol.%)/P(VDF-TrFE-CFE) binary composite to 388 MV m^{-1} of the ternary composite at room temperature (Supplementary Fig. 15).

Electrocaloric effect. Figure 3a, b and Supplementary Figs. 17, 18 summarize the EC responses including ΔT and ΔS, and EC strength ($\Delta T/E$ and $\Delta S/E$) under different electric fields. It is found that the ECE of P(VDF-TrFE-CFE) is stable in the temperature range of 0–40 °C (Fig. 3a, b and Supplementary Fig. 17). When the temperature exceeds 60 °C, Joule heat generated during the high-field half EC cycle becomes evident, as illustrated by the orange area between the heat flow curve and the baseline (Supplementary Fig. 19), and consequently, offsets the EC cooling energy and results in a significant reduction of ECE (Supplementary Note 3). For instance, at 150 MV m^{-1}, the ECE (i.e., ΔT of 4.6 °C and ΔS of 0.035 J cm^{-3} °C^{-1}) of P(VDF-TrFE-CFE) at 80 °C is only about half of that at room temperature (Fig. 3a, b and Supplementary Fig. 17). Theoretically, relaxor ferroelectric with a wide span of phase transition such as P(VDF-TrFE-CFE) should preserve the room-temperature ECE at elevated temperatures without taking into account conduction loss[24,37,38].

The binary composites with PCBM exhibit stable ECE up to 80 °C, which is nearly double that of the polymer measured at 150 MV m^{-1} and 80 °C (Fig. 3b and Supplementary Fig. 17). Although the binary BST (9 vol.%)/P(VDF-TrFE-CFE) composite shows much improved room-temperature ECE, e.g., the increase of ΔT and ΔS from 3.4 °C and 0.031 J cm^{-3} °C^{-1} of the polymer to 7.4 °C and 0.077 J cm^{-3} °C^{-1} of the composite, respectively, at 75 MV m^{-1}, its ECE decreases sharply with the applied field and temperature. For instance, at 80 °C and 150 MV m^{-1}, the binary composite displays a ΔT of 2.5 °C and a ΔS of 0.022 J cm^{-3}°C^{-1}, which is even inferior to those of the pristine polymer (Supplementary Note 3). Remarkably, the ternary composite with synergistic effect of PCBM and BST NFs exhibits desirable ECE, e.g., a ΔT of ~18.0 °C and a ΔS of 0.170 J cm^{-3} °C^{-1} at 150 MV m^{-1}, over a

https://doi.org/10.1038/s41467-024-51147-6

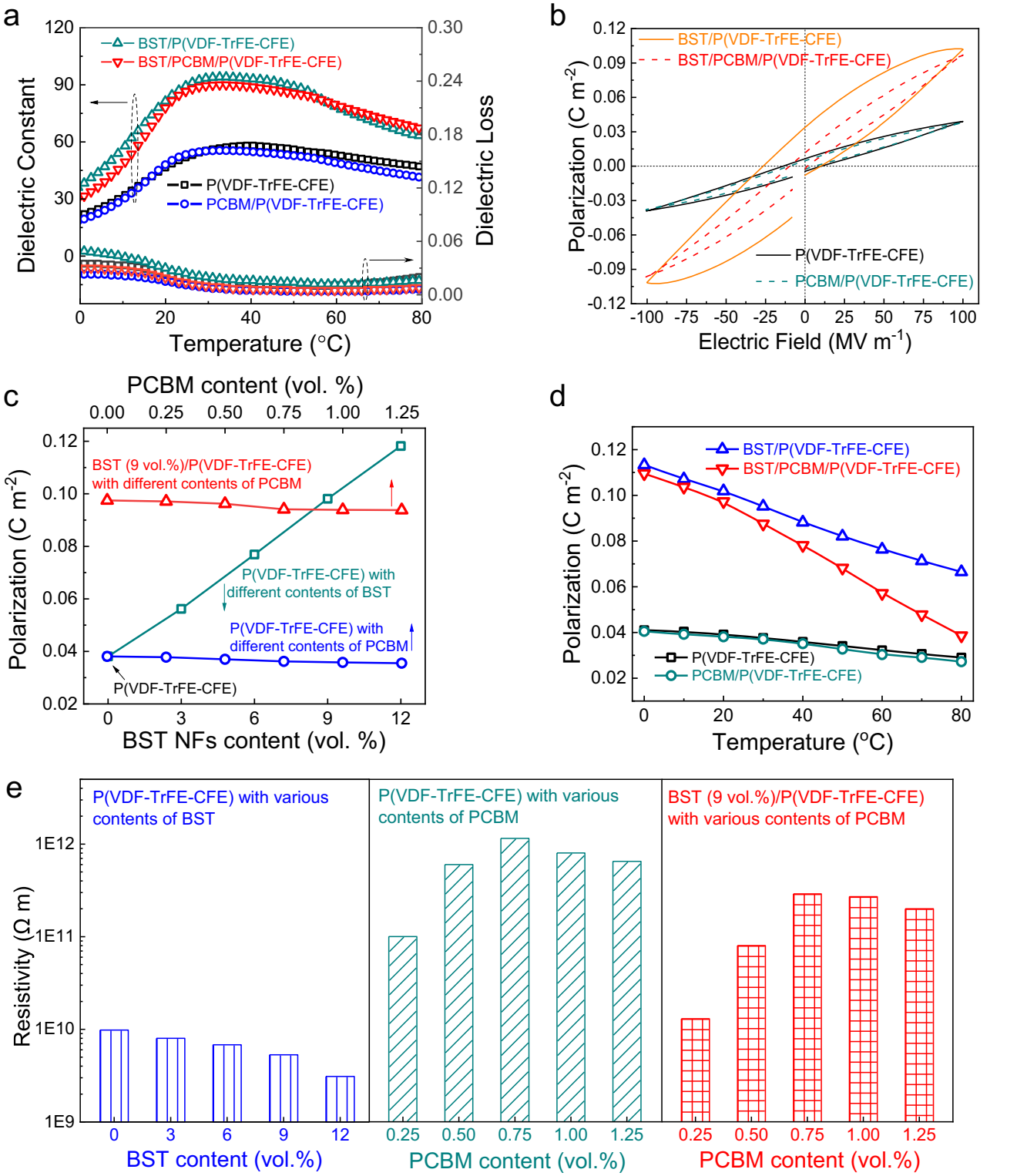

Fig. 1 | Dielectric and ferroelectric properties. a Temperature-dependent dielectric constants and losses of P(VDF-TrFE-CFE), PCBM (0.75 vol.%)/P(VDF-TrFE-CFE), BST (9 vol.%)/P(VDF-TrFE-CFE), and BST (9 vol.%)/PCBM (0.75 vol.%)/P(VDF-TrFE-CFE) @ 1 kHz. **b** *P-E* loops at room temperature. **c** Polarization of P(VDF-TrFE-CFE) and its composites with various contents of BST and PCBM at 100 MV m^{-1}. **d** Polarization of the samples as a function of temperature at 100 MV m^{-1}. **e** Room-temperature resistivity of the specimens with different contents of BST and PCBM at 100 MV m^{-1}.

temperature range of 0–80 °C (Fig. 3b and Supplementary Fig. 17). This is the highest ECE reported so far in ferroelectric ceramics, polymers and composites up to 80 °C (Fig. 3c and Supplementary Table 3). Uniform EC performance has been demonstrated in the ternary composite films (Supplementary Fig. 20).

The impact of Joule heating is also manifested in the cycling stability of the EC polymers. As shown in Supplementary Fig. 21, the binary and ternary composites with PCBM maintain the original level of ECE without decay at 150 MV m^{-1} and 80 °C after 100,000 cycles. In comparison, attenuated ECE is observed in BST/P(VDF-TrFE-CFE) when

https://doi.org/10.1038/s41467-024-51147-6

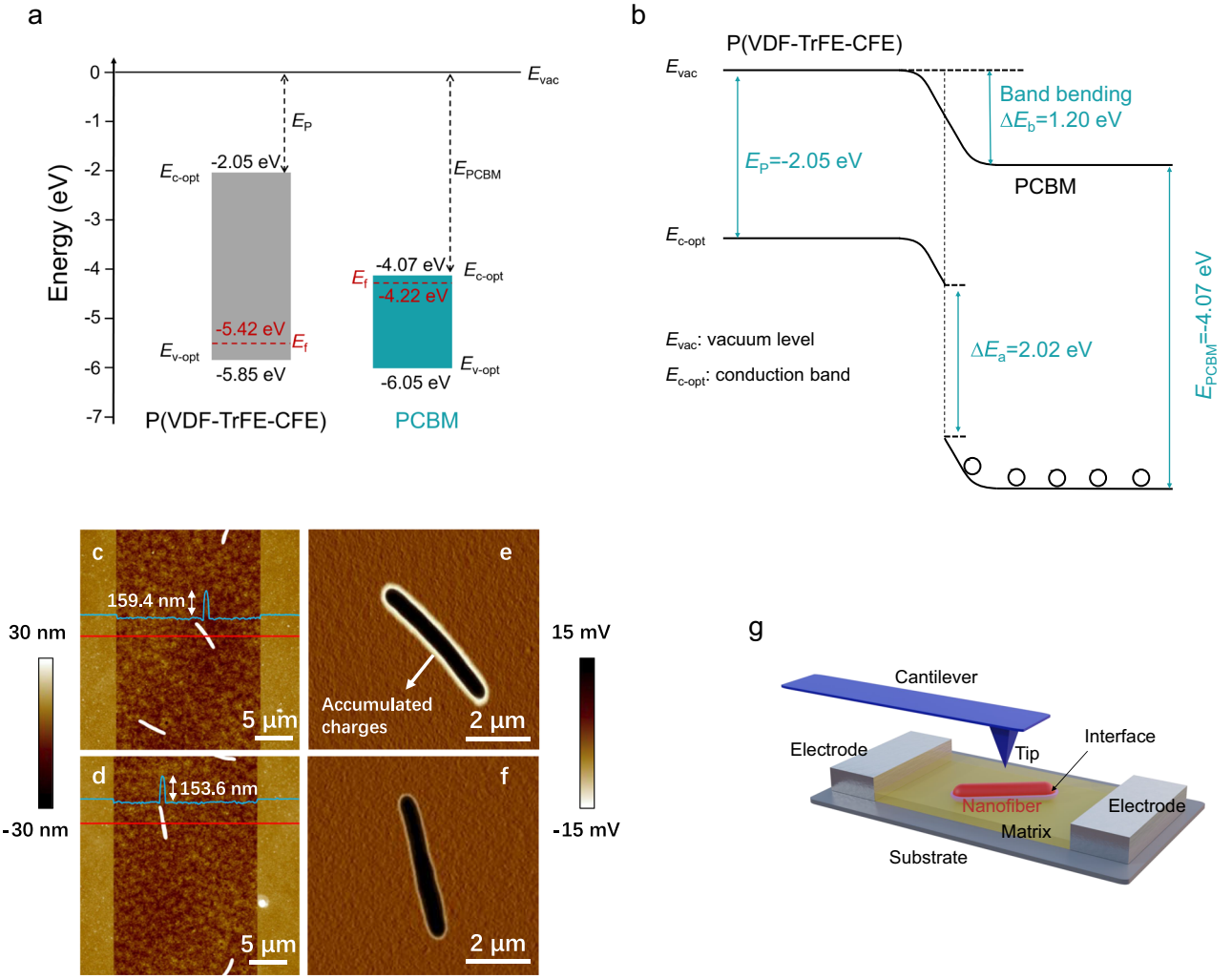

Fig. 2 | Energy band structure and charge dispersion of the composites. **a** Energy band diagram of P(VDF-TrFE-CFE) and PCBM. E_{vac} is the vacuum level, E_P and E_{PCBM} are the electron affinity of P(VDF-TrFE-CFE) and PCBM, and $E_{c\text{-}opt}$ and $E_{v\text{-}opt}$ are the optical conduction band and the optical valence band, respectively. **b** Energy band structure of PCBM-P(VDF-TrFE-CFE) interface. ΔE_a is the LUMO gap between P(VDF-TrFE-CFE) and PCBM. When P(VDF-TrFE-CFE) contacts PCBM, the equilibrium Fermi level tends to be flattened, leading to a band bending (ΔE_b = 1.20 eV) at their interface. **c**, **d** AFM topographies of the BST composites without and with PCBM, respectively. **e**, **f** Surface potential mapping of the BST NFs-P(VDF-TrFE-CFE) interfaces of the composites without and with PCBM, respectively. **g** Schematic diagram of AFM testing. A lateral electric field was applied by the pair of electrodes in the diagram, and then the AC voltage of KPFM testing was added to the tip after the lateral voltage was removed (see "Method").

subjected to the cyclic measurement even at ambient temperature, in which the Joule heat increases with the recycling process owing to the reduced resistivity (Supplementary Fig. 22).

Breakthroughs in ECE have been recently achieved in ferroelectric polymers. For example, by converting part of the chlorofluoroethylene groups into covalent double bonds, the polarizability of P(VDF-TrFE-CFE) can be enhanced, yielding a favorable ECE[21], e.g., a ΔT of 7.5 °C at a relatively low electric field of 50 MV m^{-1}. The polar conformations at the heterogeneous interface of P(VDF-TrFE-CFE) have been assembled with the organic crystal dimethylhexynediol as a sacrificial master. The same ECE (a ΔT of ~18 °C) as our ternary composite is obtained at a lower electric field of 100 MV m^{-1} at room temperature[22]. However, these newly developed ferroelectric polymers can only operate at temperatures ≤60°C because of the lack of charge capture and trap mechanisms to depress the conduction loss and maintain their high ECE at elevated temperatures.

Pyroelectric energy harvesting. The enhanced $|\partial P/\partial T|$ of the composites due to BST NFs (Fig. 1d) also benefits their pyroelectricity as the pyroelectric parameter $\pi = \partial P/\partial T$[39]. The pyroelectric effect is based on the temperature dependence of the polarization and offers a promising solid-state approach for harvesting thermal energy into electricity with the Olsen cycle[40] (Supplementary Fig. 23). We first evaluate the pyroelectric energy density of the polymer and its composites according to the *P-E* loops (Supplementary Fig. 10). Figure 3d shows the pyroelectric energy densities of the samples heated from 25 °C to different final temperatures. The introduced PCBM fillers slim the *P-E* loops of P(VDF-TrFE-CFE) because of the depressed leakage current and generate a larger area of the loops between the room-temperature charging and high-temperature discharging curves (Supplementary Fig. 10b), thus yielding a 2.4-time improvement of the pyroelectric energy density (0.19 J cm^{-3} with a temperature span of 50 °C) compared to that of P(VDF-TrFE-CFE). Although the energy density of the BST/P(VDF-TrFE-CFE) composite reaches 0.28 J cm^{-3}, it is only ~15% of theoretical improvement in the pyroelectric energy density since the largely increased leakage current widens the *P-E* loops of the binary composite (Supplementary Fig. 10c). Subsequently, with adding PCBM and BST NFs into the polymer, the highest pyroelectric energy density of 1.72 J cm^{-3} has been obtained in the ternary composite as a result of the coincident

https://doi.org/10.1038/s41467-024-51147-6

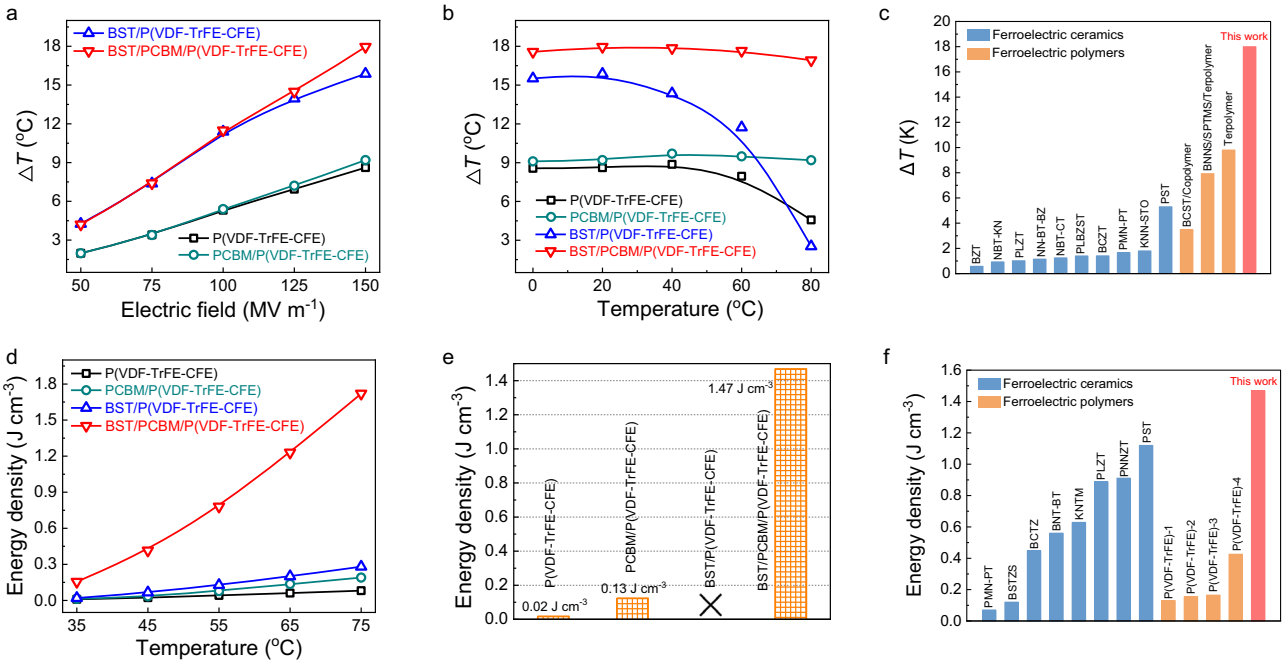

Fig. 3 | ECE and pyroelectric energy density. a ΔT of P(VDF-TrFE-CFE), PCBM (0.75 vol.%)/P(VDF-TrFE-CFE), BST (9 vol.%)/P(VDF-TrFE-CFE), and BST (9 vol.%)/PCBM (0.75 vol.%)/P(VDF-TrFE-CFE) *versus* electric fields at room temperature. **b** ΔT at different temperatures with an electric field of 150 MV m^{-1}. **c** Comparison of ΔT at ~80 °C. Detailed information for the materials is listed in Supplementary Table 3. **d** Pyroelectric energy density calculated from the *P-E* loops heated from 25 °C to different final temperatures at 100 MV m^{-1}. **e** The highest pyroelectric energy density measured from an Olsen cycle (Supplementary Fig. 19). Benefiting from their high resistivity, a field of 100 MV m^{-1} can be applied on PCBM (0.75 vol.%)/P(VDF-TrFE-CFE) and BST (9 vol.%)/PCBM (0.75 vol.%)/P(VDF-TrFE-CFE) in a temperature span of 25–75 °C, while the highest pyroelectric energy density of P(VDF-TrFE-CFE) can only be obtained at ~40 MV m^{-1} over a temperature range of 25–45 °C. The conduction loss of BST (9 vol.%)/P(VDF-TrFE-CFE) cancels out its pyroelectric energy density (Supplementary Fig. 19b). **f** Comparison of pyroelectric energy density measured from the Olsen cycle. Detailed information for the materials is listed in Supplementary Table 4.

enhancement of pyroelectric response and depression of conduction loss (Fig. 3d).

We then performed the Olsen cycle on the composites to directly measure the pyroelectric energy density[40,41]. As shown in Supplementary Fig. 24, the sample was charged with an applied field of 100 MV m^{-1} at 25 °C with a positive pulse current (A-B stage) and then heated to 75 °C under the applied field (B-C stage). Because the polarization decreases with temperature (the pyroelectric effect), a negative current should be generated during this stage. By withdrawing the electric field at 75 °C (C-D stage), the sample was further discharged with a negative pulse current. The energy density is integrated by the product of the field and current density, in which the positive and negative stages represent the charged and discharged energy densities, respectively, and the total negative value corresponds to the energy collected throughout one Olsen cycle in a unit material (see "Methods"). Operating with a temperature span of 25–75 °C and an applied field of 100 MV m^{-1}, a net energy density of 1.47 J cm^{-3} (Fig. 3e and Supplementary Figs. 24a, 26), approximately consistent with the result calculated from the *P-E* loops, is generated in the ternary composite (Supplementary Note 4). This is the state-of-the-art value, exceeding all the current ferroelectric materials, including ceramics, polymers and composites, with the same temperature span (Fig. 3f and Supplementary Table 4). In BST/P(VDF-TrFE-CFE), positive current is observed during the B-C stage because of the low resistivity of the binary composites particularly at high fields and elevated temperatures, indicating that the binary composite consumes rather than harvests energy from an Olsen cycle (Supplementary Fig. 24b). It is also noted that the ternary composites with PCBM maintain the original level of energy harvesting capability after 100,000 cycles attributable to their superior electrically insulating features[42] (Supplementary Fig. 27).

EC device for CPU cooling. We constructed an EC cooling device to cool a simulated CPU (ceramic heating plate, NO:CT-JRP, 2 cm × 2 cm). Figure 4a–c, f and Supplementary Fig. 24 show the architecture of the EC device in which heat is transported from the simulated CPU to the heat sink by the EC polymer stack themselves with electrostatic actuation. The EC stacks consist of two-layer P(VDF-TrFE-CFE) or its composites (2.5 cm × 6 cm, 25 μm thick for each layer) with inserted electrodes. With the electrostatic actuation, the polymer stack could be shuttled and attach the surfaces of the heat sink and the simulated CPU with EC heating (applying an electric field) and cooling (withdrawing an electric field), respectively[12,43]. Supplementary Movie 1 shows the electrostatic actuation of the polymer stack, and Supplementary Movie 2 presents the EC cooling process of the device with the polymer composite stacks attached to the heat source side. With a reciprocating motion, the heat of the simulated CPU could be continuously moved to the heat sink. We attached a high-precision thermocouple to the simulated CPU surface to record the temperature for comparing the cooling effect of the EC device equipped with different samples. With a heating power of 1.4 W, the temperature of the simulated CPU surface increases and reaches 80 °C in the air (Fig. 4g). The reliability of electronic chips is known to decrease by up to 10% with every 2 °C increase as the operating temperature approaches 70–80 °C[1,9].

We evaluated the EC cooling effect of the devices with two modes. In the first mode, we started the EC cooling devices with the heating power of the simulated CPU synchronously to prevent overheating. It is found that, with the applied field of 100 MV m^{-1} and an operation frequency of 1 Hz (Supplementary Fig. 30), the EC devices are capable of limiting the temperature of CPU to below 55 °C with P(VDF-TrFE-CFE) and PCBM/P(VDF-TrFE-CFE) stacks and to below 40 °C with the BST NFs-containing composite stacks (Fig. 4g). As the temperature is relatively low (<55 °C) in the whole operation process in this mode,

https://doi.org/10.1038/s41467-024-51147-6

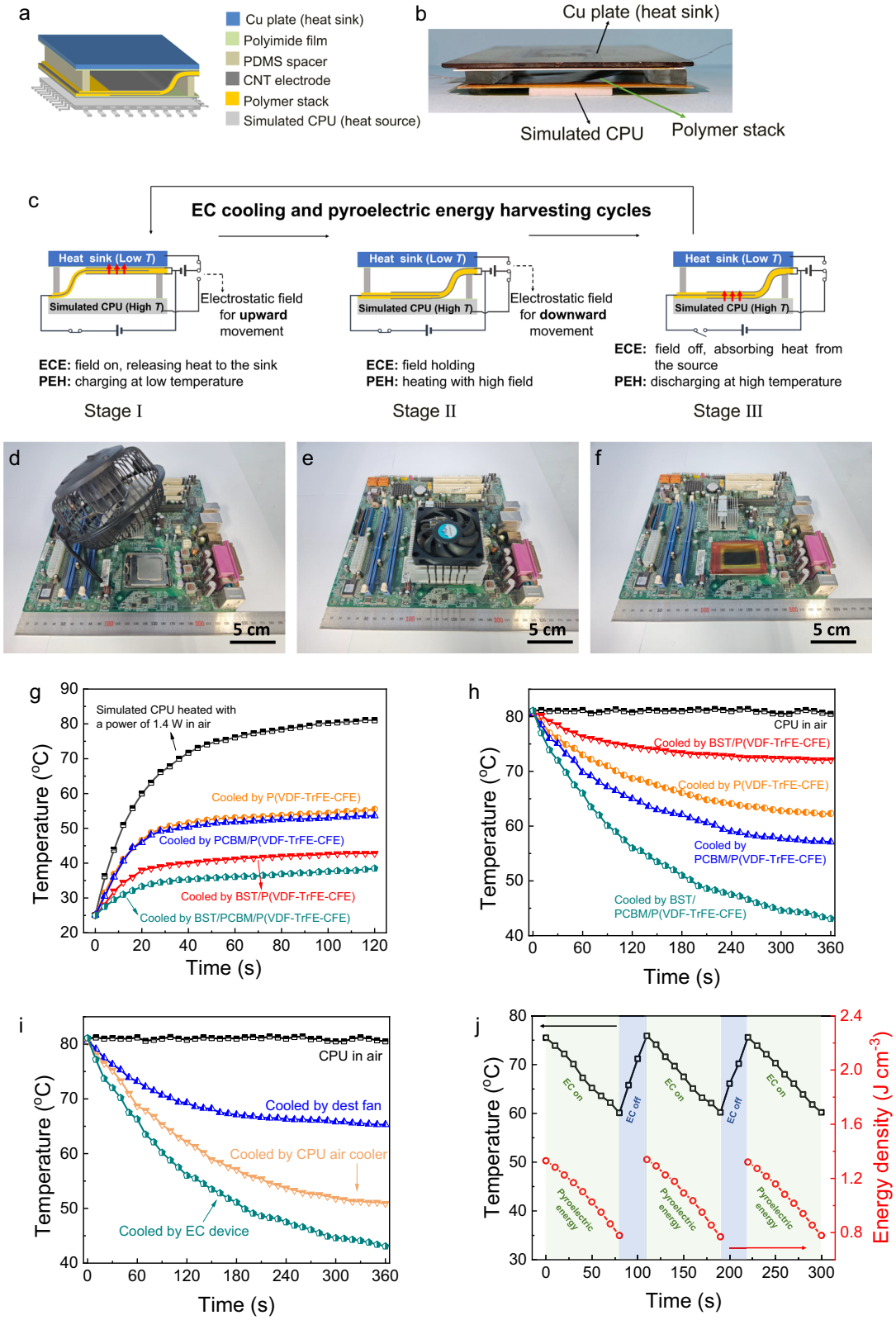

PCBM has no significant influence on the cooling capability of the devices because low Joule heat is produced in all the samples within this temperature range.

We next evaluated the performance of the EC device for cooling down an overheating chip with a continuous heating power of 1.4 W, i.e., the second mode in which the EC device is turned on after the temperature of the chip already reaches 80 °C. As summarized in Fig. 4h, while the temperature of the simulated CPU can be decreased to ~63 °C with the terpolymer EC device, the PCBM/P(VDF-TrFE-CFE) stacks can cool the CPU to a lower temperature of 56 °C. Consistent with our results on the ECE of materials, the EC device with the BST/P(VDF-TrFE-CFE) stacks has a low cooling ability and only reduces the CPU temperature to ~72 °C. This is apparently because the ECE is offset by Joule heating due to the low resistivity of the film when operating at

Fig. 4 | EC cooling and pyroelectric energy harvesting performance of the device. a Schematic of EC and pyroelectric energy harvesting device on a simulated CPU. **b** Photo of the EC and pyroelectric energy harvesting device (the size and weight of the device is shown in Supplementary Fig. 29). **c** The EC cooling combined with the pyroelectric energy harvesting (PEH) Olsen cycle for the simulated CPU. The operation process is explained in Supplementary Fig. 30 and Note 3. Photos of CPU with different thermal dissipation approaches: (**d**), Desk fan, (**e**), CPU air cooler, and (**f**), EC cooling device. The size of the EC cooling device is significantly smaller than the other two apparatuses. **g** Time-resolved temperature curves of the surface of the simulated CPU. The EC device was started with the CPU simultaneously (the EC materials are operated at 100 MV m^{-1}). Without EC cooling, the simulated CPU can be heated to 80 °C in the air with a power of 1.4 W. **h** Temperature of the surface of the simulated CPU when the EC device operating at 100 MV m^{-1} was used to cool an overheated CPU with an initial temperature of 80 °C. **i** The surface temperature of the simulated CPU (with a continuous heating power of 1.4 W) with various cooling approaches (desk fan, CPU air cooler and EC cooling device). The initial surface temperature of the simulated CPU is ~80 °C. **j** The surface temperature of the simulated CPU cooled with the EC devise and the Olsen cycle at 100 MV m^{-1}.

high temperatures (Fig. 3b, and Supplementary Fig. 17b and Movie 2). Impressively, the EC device based on the ternary polymer composite can cool down the overheated simulated CPU to 42 °C (Fig. 4h), which is superior to the desk fan and CPU air cooler (Fig. 4d–f, i). This is the demonstration that ECE can cool down an electronic device from an overheated condition while keeping the device in continuous working condition.

Pyroelectric device for CPU energy harvesting. Directly placing the polymer and composite stacks in thermal contact with the cold sink and the hot source in the EC devices also enables the utilization of the pyroelectric effect of the films to harvest thermal energy into electricity synchronously with the EC cooling process. As schematically illustrated in Fig. 4c, when attaching the heat sink, an electric field of 100 MV m^{-1} was applied on the polymer composite stack. Then, the stack attaches the simulated CPU with the electrostatic actuation, and the temperature of the film increases, e.g., to ~75 °C. Subsequently, the stack discharges at a high temperature and then returns to the heat sink with the electrostatic adsorption effect. Figure 4j shows the pyroelectric energy harvesting performance of the device with the EC cooling operation, in which the converted energy density follows the same trend of temperature through EC cooling. Notably, the energy density of 1.33 J cm^{-3} (a power density of 1.33 W cm^{-3}, Supplementary Note 5) harvested by the ternary composite over a temperature range of 25–75 °C surpasses those of the current ferroelectric ceramics, polymers and composites with the Olsen cycle. Note that this is an example of pyroelectric energy harvesting occurring simultaneously with EC cooling on electronic devices.

Discussion

We have reported the incorporation of BST NFs and PCBM into the ferroelectric polymer to form the ferroelectric polymer composites with significant EC cooling and pyroelectric energy harvesting performance for electronics operating at high temperatures. In addition to the improvement of $|\partial P/\partial T|$ that has been demonstrated in the current ferroelectric polymers and composites, a critical feature of the ternary polymer composite is to make use of PCBM to significantly enhance the electrical resistivity at high fields and elevated temperatures, which greatly benefits the ECE and pyroelectric properties and their cyclability at elevated temperatures and thus overcomes one of the major challenges in the current ferroelectric polymers. We show that ECE can be utilized to cool down an electronic device from an overheated condition while keeping the device in operation. By utilizing the designed EC device configuration, we demonstrate that, in the EC cooling process, the waste heat of working electronics can be converted synchronously into electricity through the pyroelectric properties of the composite. This work presents an effective electronic thermal management approach for control of the temperature of working electronics to avoid overheating via the ECE and simultaneous reuse of waste heat recovered from the electronic chip to decrease the energy consumption by the pyroelectric effect.

Besides the ECE and pyroelectric energy density, the heat transfer capacity determined by the thermal conductivity also influences the device performance of EC and pyroelectric energy harvesting. Ferroelectric polymers and their composites typically have much lower thermal conductivity (k, e.g., ~0.2 W m^{-1} °C^{-1}) compared to inorganic ferroelectrics (e.g., k = ~1.0 W m^{-1} °C^{-1}–2.0 W m^{-1} °C^{-1})[44,45]. Even though the giant ECE with a wide operating temperature range and the highest pyroelectric energy density have been achieved in our design, the cooling capability and the pyroelectric power density of the device are still hindered by the low heat transfer capability of the polymers and composites. Owing to the relatively low thermal conductivities, the thickness of the composite films has been designed as thin as 25 μm in this work since thicker films require longer periods for the materials to fully deliver EC cooling energy to the thermal load. As a result, the mass of the EC medium within a certain area is small, and the cooling capacity of our device is still inferior to those equipped with ferroelectric multilayer ceramic capacitors with thickness ranging from 500 to 1000 μm[14,15]. Also because of the relatively low thermal conductivity of the ferroelectric polymers, the Olsen cycle for pyroelectric harvesting has to operate with a relatively low frequency (e.g., 1 Hz in this work) in order to realize full heat exchange between the heat source/sink and the ferroelectric polymer composites. On the other hand, the Olsen cycle in inorganic ferroelectrics can be run with a high speed. For example, even with a lower energy density of 1.06 J cm^{-3} (~80% that of our ternary composite), a much higher energy power density is obtained in a lead magnesium niobate-lead titanate thin film with an operating frequency of 1 kHz[39]. The thermal conductivity of the ferroelectric polymer can be significantly improved by incorporating electrically insulating nanofillers with high thermal conductivity, e.g., boron-nitride nanosheets (BNNSs)[46,47]. It is thus believed that the thermal conduction of our composites can be improved by introducing the nanofillers with high electrical resistivities and high thermal conductivities.

The compact size and low energy consumption of the electrostatic actuation design make the device promising for integrated circuit thermal management and energy harvesting. The device performance of EC cooling and pyroelectric harvesting can be further optimized with a cascade design as shown in Supplementary Fig. 32. The device integrating multiple units of the polymer elements with a vertical cascaded connection possesses high active thermal mass and enhanced heat flux[43,48]. Therefore, the cascade design could provide improved cooling power and efficiency, and the pyroelectric energy harvesting power based on the electrostatic actuation mode.

Methods

Synthesis of the composites

BST NFs were synthesized by an electrospinning approach. Barium acetate (AR, 99.9%, Sinopharm) and strontium acetate (AR, 99.9%, Sinopharm) were weighted in stoichiometric and dissolved in acetic acid (AR, 99.9%, Sinopharm) to form a solution with a concentration of 0.12 g mL^{-1}. Meanwhile, tetrabutyl titanate (Sinopharm, CP, 98%) was dissolved in acetylacetone (AR, 99.9%, Aladdin) with a concentration of 0.3 g mL^{-1}. Then, the two solutions were mixed with poly(vinyl pyrrolidone) (PVP) (MW 1300000, Aladdin) dissolved ethanol (0.4 g mL^{-1}). Being stirred for 1 hour, the clean precursor was spined with an electrospinning machine (ET−2535X, Beijing Yongkang Leye Technology Development Co., Ltd.). The voltage between the syringe needle and

the roller collector of the electrospinning process was ~15 kV. The jetted nanofibers were collected by a roller with a rolling speed of 140 r min^{-1}. The BST NFs were obtained by annealing the filar precursors at 800 °C.

P(VDF-TrFE-CFE) (61.8/31.0/7.2) was dissolved in *N*,*N*-dimethylformamide (DMF, AR, 99.9%, Aladdin) with a concentration of 2 wt.%-6 wt.% and stirred at ~50 °C to form a clear solution. Subsequently, BST NFs were added into the solution with various compositions and stirred again for 2 h. For the composites with [6,6]-phenyl C61 butyric acid methyl ester (PCBM, AR, 99%, Aladdin), PCBM/DMF solution was added into the prepared solution with the required compositions. Thereafter, the mixtures were cast onto glass plates and dried at 40–60 °C for 24 h. After that, the films were peeled off from the glass, heated at 90 °C for 12 h and annealed at 105 °C for another 12 h in a vacuum oven.

Characterization

The phase structure of the samples was determined by X-ray diffraction (7000 S/L, Shimadzu Corp.) with Cu Kα radiation. Scanning electron microscopy (SEM, GeminiSEM 300, Zeiss) and field emission transmission electron microscope (FTEM, Talos F200X, FEI) were utilized to observe the morphology of the composites with the fillers. A differential scanning calorimeter (Diamond DSC, PerkinElmer Instruments) was used to scan the DSC curves of the polymer and its composite and acquire the specific heat as a function of temperature. Young's modulus measurement was carried out on an Instron 5866. Fourier-transform infrared spectroscopy (FTIR) was measured using Nicolet iS50R (Thermo Scientific). The detailed information for evaluating the bandgap structure of PCBM and P(VDF-TrFE-CFE) was described in Supplementary Fig. 13, in which ultraviolet photoelectron spectroscopy (UPS) and ultraviolet-visible spectrophotometer (UV-vis) were tested by AXIS SUPRA+ (Kratos) and UV-3600 Plus spectrophotometer (Shimadzu), respectively.

For the atomic force microscopy (AFM) and Kelvin probe force microscopy (KPFM) measurements, P(VDF-TrFE-CFE) was dissolved in DMF with a concentration of 5 mg·ml^{-1} and stirred over 6 h. For the composites, PCBM was added to the solution. BST NFs were dispersed with DMF by a 45-min tip-type sonication (90 W). The dispersion was cast onto a silicon substrate between two electrodes immediately after the sonication. Then the solution of P(VDF-TrFE-CFE) was cast onto the substrate and the sample was dried at 60 °C for 6 h in a vacuum oven. The thickness of the P(VDF-TrFE-CFE) matrix was controlled at approximately 180 nm, and the NFs were partially exposed to make the interface detectable. The topography, surface potential and piezo-response force microscopy (PFM) measurements were conducted on a Dimension Icon (Bruker) system. The topographies were measured in the ScanAsyst mode by SCANASYST-AIR probes. The surface potentials were measured in the KPFM mode by SCM-PIT-V2 probes. A lateral external voltage of 50 V was applied to the sample by a Keithley 6517B electrometer for 10 min. The KPFM was performed with a 5 V tip AC voltage after the lateral voltage on the sample was removed. The Nano-IR measurements were performed on an Anasys nanoIR3 (Bruker) system with a QCL source (800–1900 cm^{-1}) in tapping AFM-IR mode. The wavenumber of the test was 1728 cm^{-1}.

The dielectric spectra measurement was conducted by a Hewlett-Packard LCR (4284 A) with a temperature control system (PK-CPT1705, PolyK Technologies). Hewlett-Packard 4140B pAmeter/voltage source connected with TREK model 2210 amplifier was used to evaluate the electrical resistivity of the composites. The electric hysteresis loops were obtained by a ferroelectric tester (PK-CPE 1701, PolyK Technologies) with a modified Sawyer-Tower circuit. EC performance was measured using a heat flux method, and the details are described in Supplementary Fig. 33. The infrared movies were captured by an infrared camera (T420, FLIR). The pyroelectric energy density with the Olsen cycle was evaluated by a pyroelectric energy harvesting system (PYEC-1000, Wuhan Yanhe Technology Co., Ltd.). The system consists of temperature control and voltage-current applying/monitoring modules. To run the Olsen cycle, the system first applied a high field on the material and then increased its temperature by the temperature control module. When the temperature reached the preset temperature, the sample was discharged. During the whole process, the voltage (V), current (I) and temperature (T) were monitored by the system. The pyroelectric energy density was obtained with the formula $D_p = \frac{1}{v}\int_0^t V \cdot I\mathrm{d}t = \int_0^t E \cdot J\mathrm{d}t$, where E, J, v and t are the electric field, current density, volume of the sample, and time for the Olsen cycle, respectively, and the total negative value of D_p represents the energy density harvested by the specimen with one Olsen cycle (Supplementary Fig. 24).

EC and energy harvesting devices

Figure 4a, c schematically shows the structure and working mechanism of the EC cooling and pyroelectric energy harvesting device based on a two-layer composite stack. The simulated CPU (ceramic heating plate, NO:CT-JRP) functioned as a heat source. The heat source and heat sink were attached to the bottom and top sides with two spacers (polydimethylsiloxane, PDMS) to construct the device. The polymer stack was bent into an S-shape and fixed onto the PDMS spacers. The two-layer stack was hot pressed by two polymer films with interlayer electrodes made of Carbon nanotubes (purity >90%, XFNANO) conductive network. Thin silver wires were attached to the electrodes to provide electric fields for the ECE, pyroelectric energy harvesting (Olsen cycle) and electrostatic actuation (Supplementary Movies 1 and 2). For comparisons, the simulated CPU was also cooled with a desk fan and CPU air cooler. The desk fan (COMIX L602, 5 V, 0.5 A, 2.5 W) in Fig. 4d has a size of $\Phi 15 \times 8$ cm^3 and a flow rate of 2.14 m s^{-1}. The CPU air cooler ((DELTA-AFB0705HB, 5 V, 0.2 A, 1 W)) in Fig. 4e has a size of $5 \times 9 \times 8$ cm^3 and a flow rate of 0.49 m s^{-1}. The heat sink consists of a bottom aluminum block and a top fan. When dissipating heat, the heat sink is tightly attached to the heat source with a heat transfer area of 2×2 cm^2.

Data availability

All data supporting this study and its findings are available within the article and its Supplementary Information. Source data are provided with this paper.

References

1. Zhang, Z., Wang, X. & Yan, Y. A review of the state-of-the-art in electronic cooling. *e-Prime - Adv. Electr. Eng., Electron. Energy* **1**, 100009 (2021).
2. Garimella, S. V., Persoons, T., Weibel, J. A. & Gektin, V. Electronics thermal management in information and communications technologies: challenges and future directions. *IEEE Trans. Compon. Packag. Manuf. Technol.* **7**, 1191–1205 (2017).
3. Gebrael, T. et al. High-efficiency cooling via the monolithic integration of copper on electronic devices. *Nat. Electron.* **5**, 394–402 (2022).
4. He, Z., Yan, Y. & Zhang, Z. Thermal management and temperature uniformity enhancement of electronic devices by micro heat sinks: A review. *Energy* **216**, 119223 (2021).
5. Fleischer, A. S. Cooling our insatiable demand for data. *Science* **370**, 783–784 (2020).
6. Erp, R., Soleimanzadeh, R., Nela, L., Kampitsis, G. & Matioli, E. Co-designing electronics with microfluidics for more sustainable cooling. *Nature* **585**, 211–216 (2020).
7. Khosla, R. et al. Cooling for sustainable development. *Nat. Sustainability* **4**, 201–208 (2021).
8. Li, M. D. et al. Thermal management of chips by a device prototype using synergistic effects of 3-D heat-conductive network and electrocaloric refrigeration. *Nat. Commun.* **13**, 5849 (2022).

9. Gan, T., Ming, T., Fang, W., Liu, Y. & Ahmadi, M. H. Heat transfer enhancement of a microchannel heat sink with the combination of impinging jets, dimples, and side outlets. *J. Therm. Anal. Calorim.* **141**, 45–56 (2020).
10. Moya, X. & Mathur, N. D. Caloric materials for cooling and heating. *Science* **370**, 797–803 (2020).
11. Hou, H., Qian, S. & Takeuchi, I. Materials, physics and systems for multicaloric cooling. *Nat. Rev. Mater.* **7**, 633–652 (2022).
12. Ma, R. et al. Highly efficient electrocaloric cooling with electrostatic actuation. *Science* **357**, 1130–1134 (2017).
13. Sungtaek, Ju,Y. Solid-state refrigeration based on the electrocaloric effect for electronics cooling. *J. Electron. Packag.* **132**, 041004 (2010).
14. Wang, Y. et al. A high-performance solid-state electrocaloric cooling system. *Science* **370**, 129–133 (2020).
15. Li, J. et al. High cooling performance in a double-loop electrocaloric heat pump. *Science* **382**, 801–805 (2023).
16. Plaznik, U. et al. Bulk relaxor ferroelectric ceramics as a working body for an electrocaloric cooling device. *Appl. Phys. Lett.* **106**, 043903 (2015).
17. Nair, B. et al. Large electrocaloric effects in oxide multilayer capacitors over a wide temperature range. *Nature* **575**, 468–472 (2019).
18. Nouchokgwe, Y. et al. Giant electrocaloric materials energy efficiency in highly ordered lead scandium tantalite. *Nat. Commun.* **12**, 3298 (2021).
19. Shi, J. et al. Electrocaloric Cooling materials and devices for zero-global-warming potential, high-efficiency refrigeration. *Joule* **3**, 1–26 (2019).
20. Torelló, A. & Defay, E. Electrocaloric coolers: A review. *Adv. Electron. Mater.* **8**, 2101031 (2022).
21. Qian, X. et al. High-entropy polymer produces a giant electrocaloric effect at low fields. *Nature* **600**, 664–669 (2021).
22. Zheng, S. et al. Colossal electrocaloric effect in an interface-augmented ferroelectric polymer. *Science* **382**, 1020–1026 (2023).
23. Qian, J. et al. Interfacial coupling boosts giant electrocaloric effects in relaxor polymer nanocomposites: In situ characterization and phase-field simulation. *Adv. Mater.* **31**, 1801949 (2019).
24. Li, X. et al. Tunable temperature dependence of electrocaloriceffect in ferroelectric relaxor poly(vinylidenefluoride-trifluoroethylene-chlorofluoroethylene terpolymer. *Appl. Phys. Lett* **99**, 052907 (2011).
25. Gong, J. & McGaughe, A. J. H. Device-level thermodynamic model for an electrocaloric cooler. *Int. J. Energy Res.* **44**, 5343–5359 (2020).
26. Gu, H. et al. A chip scale electrocaloric effect based cooling device. *Appl. Phys. Lett.* **102**, 122904 (2013).
27. Lu, S. et al. Joule heating-A significant factor in electrocaloric effect. *Ceram. Int.* **45**, 16992–16998 (2019).
28. Lu, S. G. et al. Comparison of directly and indirectly measured electrocaloric effect in relaxor ferroelectric polymers. *Appl. Phys. Lett.* **97**, 202901 (2010).
29. Weyland, F. et al. Criticality: concept to enhance the piezoelectric and electrocaloric properties of ferroelectrics. *Adv. Funct. Mater.* **26**, 7326–7333 (2016).
30. Li, Z. et al. Effects of thermal and electrical hysteresis on phase transitions and electrocaloric effect in ferroelectrics: A computational study. *Acta Mater.* **228**, 117784 (2022).
31. Pirc, R., Kutnjak, Z., Blinc, R. & Zhang, Q. M. Electrocaloric effect in relaxor ferroelectrics. *J. Appl. Phys.* **110**, 074113 (2011).
32. Liu, Y., Scott, J. F. & Dkhil, B. Some strategies for improving caloric responses with ferroelectrics. *Apl. Mater.* **4**, 064109 (2016).
33. Zhou, Y. et al. Giant polarization ripple in transverse pyroelectricity. *Nat. Commun.* **14**, 426 (2023).
34. Li, H., Bowen, C. R., Dan, H. & Yang, Y. Pyroelectricity induced by schottky interface above the curie temperature of bulk materials. *Joule* **8**, 401–415 (2024).
35. Yuan, C. et al. Polymer/molecular semiconductor all-organic composites for high-temperature dielectric energy storage. *Nat. Commun.* **11**, 3919 (2020).
36. Peng, S. et al. Mapping the space charge at nanoscale in dielectric polymer nanocomposites. *ACS Appl. Mater. Interfaces* **12**, 53425–53434 (2020).
37. Shi, Y. P. & Soh, A. K. Modeling of enhanced electrocaloric effect above the Curie temperature in relaxor ferroelectrics. *Acta Mater.* **59**, 5574–5583 (2011).
38. Li, Q. et al. Relaxor ferroelectric-based electrocaloric polymer nanocomposites with a broad operating temperature range and high cooling energy. *Adv. Mater.* **27**, 2236–2241 (2015).
39. Pandya, S. et al. Pyroelectric energy conversion with large energy and power density in relaxor ferroelectric thin films. *Nat. Mater.* **17**, 432–438 (2018).
40. Olsen, R. B., Bruno, D. A., Briscoe, J. M. & Jacobs, E. W. Pyroelectric conversion cycle of vinylidene fluoride-trifluoroethylene copolymer. *J. Appl. Phys.* **57**, 5036–5042 (1985).
41. Lheritier, P. et al. Large harvested energy with non-linear pyroelectric modules. *Nature* **609**, 718–721 (2022).
42. Zhang, C., Zeng, Z., Zhu, Z., Karami, M. & Chen, X. Impact of leakage for electricity generation by pyroelectric converter. *Phys. Rev. Appl.* **14**, 064079 (2020).
43. Meng, Y. et al. A cascade electrocaloric cooling device for large temperature lift. *Nat. Energy* **5**, 996–1002 (2020).
44. Yu, J. et al. Permittivity, thermal conductivity and thermal stability of poly (vinylidene fluoride)/graphene nanocomposites. *IEEE Trans. Dielectr. Electr. Insul.* **18**, 478–484 (2011).
45. Yoshida, I. Thermal conduction in ferroelectric ceramics. *J. Phys. Soc. Jpn.* **15**, 2211–2219 (1960).
46. Han, D. et al. Molecular interface regulation enables order-disorder synergy in electrocaloric nanocomposites. *Joule* **7**, 2174–2190 (2023).
47. Zhang, G. et al. Ferroelectric polymer nanocomposites with complementary nanostructured fillers for electrocaloric cooling with high power density and great efficiency. *ACS Appl. Energy Mater.* **1**, 1344–1354 (2018).
48. Bo, Y. et al. Electrostatic actuating double-unit electrocaloric cooling device with high efficiency. *Adv. Energy Mater.* **11**, 2003771 (2021).

Acknowledgements

This work is supported by the National Natural Science Foundation of China (grant nos. 52172114, 52372108, 92166203, 52272110, 62105110 and 523B2011) (G.Z., S.J., Q.L., K.L., and F.L.) and the National Key Research and Development Program of China (2022YFA1204603) (G.Z., and K.L.). We also would like to thank the Analytical and Testing Center of HUST.

Author contributions

G.Z. conceived the idea. G.Z., S.J., R.M., Q.L. and Q.W. supervised the project. G.Z., R.M., Q.L., K.L., K.Z., and F.L. designed the experiments. K.Z., K.L., L.L. and F.L. prepared the polymer composites and performed the characterizations. Q.L. and J.L. conducted the AFM and KPFM measurements. R.M., G.Z. P.B. and K.Z. designed the EC cooling and pyroelectric energy harvesting devices. K.Z. P.B., F.L. and K.L. carried out the device fabrication and characterizations. G.Z. and Q.W. prepared the manuscript, with input from all authors.

Competing interests

The authors declare no competing interests.

Additional information

Supplementary information The online version contains supplementary material available at https://doi.org/10.1038/s41467-024-51147-6.

Correspondence and requests for materials should be addressed to Rujun Ma, Qi Li, Qing Wang or Guangzu Zhang.

Peer review information *Nature Communications* thanks Haolun Wang, and the other, anonymous, reviewers for their contribution to the peer review of this work. A peer review file is available.